Frontiers in Heat and Mass Transfer

Tech Science Press

https://doi.org/10.32604/fhmt.2026.076167

ARTICLE

Numerical Analysis of Heat Transfer Characteristics in the Thermal-Transfer Printing Head under Pulse Heating Conditions

Xiufeng Fei[1], Jian Liu[1,2], Dianhang Wei[1,*] and Xiaosong Zhang[1,2,*]

[1]School of Energy & Environment, Southeast University, Nanjing, China
[2]Engineering Research Center of Building Equipment, Energy, and Environment, Ministry of Education, Nanjing, China
*Corresponding Authors: Dianhang Wei. Email: dianyangwei@163.com; Xiaosong Zhang. Email: rachpe@seu.edu.cn

Received: 15 November 2025; Accepted: 22 January 2026; Published: 30 April 2026

ABSTRACT: Thermal-transfer printing technology has gained widespread adoption in small-format printing devices owing to its fast printing speed, good image quality, and environmental sustainability. However, scaling this technology to large-format printing equipment remains challenging, primarily because the internal heat transfer mechanisms in the large-scale thermal-transfer printing head (TPH) are not yet fully understood. This knowledge gap limits further optimization of device design. A two-dimensional model was established to numerically investigate the internal heat transfer within the thermal-transfer printing head under pulse heating conditions. The simulations reveal that the internal temperature distribution adopts a star-like pattern, driven by the higher thermal conductivity of the bottom film, which accelerates temperature changes. The printing paper effectively filters the heat fluctuation from the heat generator due to its high specific heat capacity and low thermal conductivity. Parametric analysis demonstrates that the temperature of the heat generator reaches a maximum of 428°C at 70% of pulse width modulation and 500°C at an amplitude of 5.04 kW. These findings provide a theoretical foundation for optimizing large-scale thermal-transfer printing systems.

KEYWORDS: Heat transfer; thermal-transfer print; heat conductivity; pulse heat; numerical simulation; parametric study

1 Introduction

Over the years of development, printing devices have become an integral part of people's work and life [1,2]. To meet the increasingly sophisticated printing demands, a variety of printing technologies have emerged. So far, the printing technology is primarily categorized into laser print [3–6], inkjet print [7,8], and thermal-transfer print [9–11], according to the different printing methods.

The thermal-transfer printer is a common printing device. Its printing principle is shown in Fig. 1. After the thermal-transfer printing head (TPH) heats the ribbon, the pigment attached to the ribbon melts and is then transferred to the printing medium. As the ribbon moves in tandem with the printing medium, the final text and image are rendered on the printing medium. This mechanism enables thermal-transfer printing devices to achieve lightweight and portable designs while maintaining high speed and high image quality [12]. In the broad market application prospects, developing better printing performance, low-cost and environmentally friendly thermal-transfer printing technologies has attracted considerable attention [13–15].

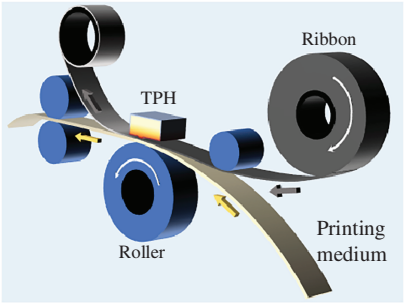

Figure 1: Diagram of the thermal-transfer printing mechanism.

Research efforts have pursued two main directions. On the one hand, some scholars have researched printing ink materials to broaden the application scenarios of thermal-transfer printing technology [16]. Kitamura [17] used laser-heated sublimation dye-transfer printing technology to prepare multi-colored ink sheets for color-printed images with high resolution and good continuous step reproducibility. Fe-doped liquid metal conductive ink can be efficiently transferred to a special substrate for the thermal-transfer printing process, as the hydrogen bonding between the liquid metal and the fructose layer can be broken at around 80°C [18]. Yang et al. [19] and Luo et al. [20] proposed a class of alcohol-resistant thermal-transfer printing inks and made this class of printing inks to hold a wide printing temperature range.

On the other hand, researchers have investigated the contact situation between the TPH and the ribbon to improve the performance of thermal-transfer printers. Nitta et al. [21] analyzed the variation in contact pressure between the TPH and the ink ribbon. Maximum contact pressure was found to occur behind the heating spot by calculating with a three-dimensional Maxwell model, which implies that the wear is potentially greatest in this area. To assess the influence of the sprayed surface on heat transfer, Irii et al. [22] reported the distribution of the contact pressure of the TPH with the surface concavity using the finite element method. Fukue et al. [23] and Hirose et al. [24] focused on the heat transfer from TPH to the printing paper and analysis of the temperature response of the printing paper. It is found that the temperature response is greatly affected by the paper's thermophysical properties and contact thermal resistance.

The literature review reveals that most studies focus on external aspects of the printhead, leaving the internal heat transfer process between the various components unexplored when a heat source operates within the TPH. In addition, some studies have attempted to use large-scale thermal-transfer printers for banner printing, leveraging the eco-friendly and energy-saving advantages of thermal-transfer printing technology [25]. Nevertheless, this could cause changes in the TPH and the printing medium, resulting in internal heat transfer characteristics that may differ from those of a small thermal-transfer printing device.

Therefore, we have built a computational model to reveal the internal heat transfer pattern when the TPH is on a large scale. The temperature distribution and the temperature of each component in the TPH are deeply analyzed under the pulse heating condition. Moreover, the influence of the two essential parameters-pulse width modulation (PWM) and amplitude-on the heat transfer performance in the pulse heating process is explored. This study is expected to provide a certain theoretical basis for the structural design of future large-scale thermal transfer printing devices.

2 Simulation

2.1 Fabrication of the Thermal-Transfer Printer

A typical thermal-transfer printer resembles a sandwich structure, as shown in Fig. 2. From top to bottom, it comprises an aluminum layer, a ceramic plate, a glass substrate, a string of heat generators, two protective films, and a piece of paper with pigment. The other components, except the bottom papers, consist of a TPH. The heat generator, consisting of numerous hot spots in series, is embedded within the glass substrate. Thermophysical properties of the main components are listed in Table 1. The listed thermal conductivity values are those in the through-thickness direction (y-direction in the model), which is the primary direction of heat flow from the TPH to the paper. The materials (aluminum, ceramic, glass) are assumed to be isotropic for this analysis.

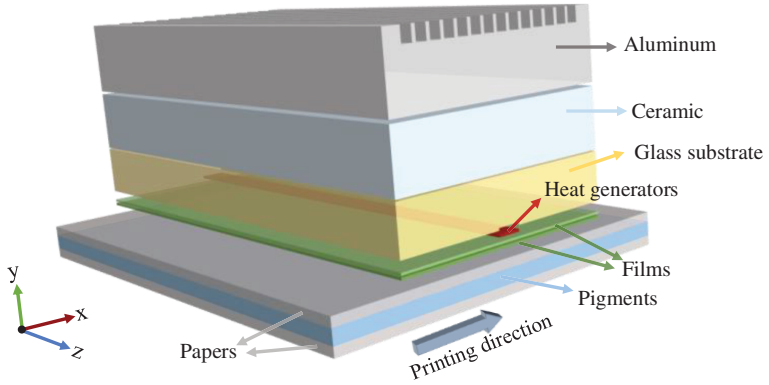

Figure 2: The structure of a typical TPH with printing medium.

Table 1: Thermophysical properties of main components.

Component	Density ($kg \cdot m^{-3}$)	Specific Heat Capacity ($J \cdot kg^{-1} \cdot K^{-1}$)	Thermal Conductivity ($W \cdot m^{-1} \cdot K^{-1}$)
Aluminum plate	2688.9	902	237
Ceramic plate	3970	765	16
Glass substrate	2500 [26]	820	1.1
Heat generator	8960	384	401
Protective film A	2870	1050	5.77
Protective film B	2900 [27]	800	400
Paper	700 [28]	1200	0.12

The paper with the pigment moves along the x-axis at a constant speed during the practical printing process. Meantime, the heat generated by the heat generator is transferred to the paper and melts the pigment attached to the paper. Then, the pigment becomes liquid and drops onto the paper to form a pattern. It is worth noting that when the device is in operation, there is a thermal conductivity within the TPH and a phase-change heat transfer after the pigment is heated. Since this paper focuses on the heat transfer process inside the TPH, we replaced the phase-change heat transfer of pigment with the convection heat transfer of air to simplify the model calculation. This modeling approach is supported by prior work. According to the Cui's study [28], replacing the pigment layer with an air gap and focusing on the heat flux arriving at the paper-air interface has been shown to yield simulation results that align well with experimental

temperature measurements at key points within the TPH structure. This indicates that for analyzing the internal temperature distribution and transient response of the TPH itself, the simplification is valid and captures the dominant physics. Therefore, after the pigment is replaced with the air in the modelling process, the papers in Fig. 2 are held, and only the air flows uniformly.

Furthermore, each hot spot is the same size, while the length of every hot spot along the z-axis direction is tiny relative to the length of the entire heater. Consequently, the thermal conductivity of any hot spot in the z-axis direction could be ignored as the heating power of all hot spots is kept the same. On the other hand, it is more critical to analyze the heat transfer characteristics of the thermal-transfer printer on the x-y plane, as shown in Fig. 3. In the modelling process, the origin is set at the lower left corner of the glass substrate, and the directions of the x- and y-axes are also indicated in Fig. 3. The dimensions of each part in the x-y plane are listed in Table 2.

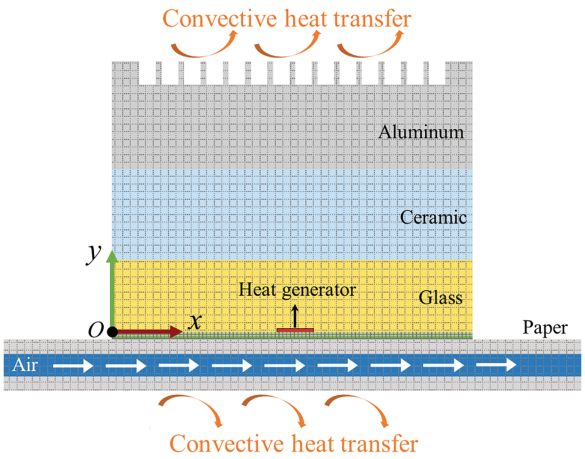

Figure 3: Cross section of the thermal-transfer printer.

Table 2: Components' dimensions in the x-y plane.

Component	Length (mm)	Height (mm)
Aluminum plate	30	20
Ceramic plate	30	10
Glass substrate	30	3
Heat generator	0.2	0.01
Protective film A	30	0.004
Protective film B	30	0.006
Paper	100	0.3
Air tunnel	100	0.4

2.2 Mathematical Model

For the two-dimension model introduced in Fig. 3, several assumptions are made: (i) The influence of thermal radiation is ignored, (ii) Heat flow and temperature are continuous at the interfaces between materials, (iii) Air between the papers is laminar because the Reynolds number for air flowing at 0.1 $m \cdot s^{-1}$ is 5 (<<2300). (iv) The thermophysical properties of different materials remain stable, (v) Gravity force is considered [29].

Based on the above assumptions, the governing equations referred in this work is shown as follows:

Energy equation of air:

$$\frac{\partial T}{\partial t} + u\frac{\partial T}{\partial x} + v\frac{\partial T}{\partial y} = \alpha\left(\frac{\partial^2 T}{\partial x^2} + \frac{\partial^2 T}{\partial y^2}\right) \tag{1}$$

where T and t represent temperature and time, while u and v are the velocity components of the air in the x and y directions, respectively.

Conduction equation:

$$\frac{\partial T}{\partial t} = \alpha\left(\frac{\partial^2 T}{\partial x^2} + \frac{\partial^2 T}{\partial y^2}\right) + \frac{\dot{\Phi}}{\rho c} \tag{2}$$

where α, $\dot{\Phi}$, ρ, and c respectively represent the thermal diffusivity, the heat source, the density, and the specific heat capacity.

Continuity equation:

$$\frac{\partial u}{\partial x} + \frac{\partial v}{\partial y} = 0 \tag{3}$$

Momentum equations in two dimensions:

$$\frac{\partial u}{\partial t} + u\frac{\partial u}{\partial x} + v\frac{\partial u}{\partial y} = -\frac{1}{\rho}\frac{\partial P}{\partial x} + \frac{u}{\rho}\left(\frac{\partial^2 u}{\partial x^2} + \frac{\partial^2 u}{\partial y^2}\right) \tag{4}$$

$$\frac{\partial v}{\partial t} + u\frac{\partial v}{\partial x} + v\frac{\partial v}{\partial y} = -\frac{1}{\rho}\frac{\partial P}{\partial y} + \frac{u}{\rho}\left(\frac{\partial^2 v}{\partial x^2} + \frac{\partial^2 v}{\partial y^2}\right) \tag{5}$$

where P is the air pressure.

Fluent is a finite-volume based solver that discretizes and iteratively solves the system of Eqs. (1)–(5), and the solution algorithm chosen is SIMPLEC. The initial temperature of the TPH, papers, and air is set to 30°C. The air flows along x positive direction as shown in Fig. 3, of which the volume flowrate is set at 0.06 $m{\cdot}s^{-1}$. The top and bottom of the model in Fig. 3 are defined as convective heat transfer boundaries with a convective heat transfer coefficient of 5 $W{\cdot}m^{-2}{\cdot}K^{-1}$, while the other boundaries conform to the adiabatic condition. The solution is considered converged when the scaled residuals for all governing equations fell below 10^{-6}.

2.3 Grid Independence and Model Verification

The grid of the model is meshed through Ansys Mesh module. Since the number of meshes has a significant effect not only on the accuracy of the simulation results, but also on the computation time. Although the shape of each part is rectangular, a large area difference among components exists in this work. Therefore, each component is meshed reasonably separately to maintain the fast convergence of the calculation process. The two films and heat generator are treated with more detailed meshing. We set up six groups of different grid quantities to select the optimal number of meshes. When the heat generator heats up with 3.6 kW for 0.05 s, the temperature of the point located at (15 mm, −0.31 mm) varying with different grid quantities is recorded, as shown in Fig. 4. Temperature changes become negligible when the grid quantity exceeds 80,000. As a result, the appropriate number of grids is 104,723, considering improving the calculation speed while ensuring the calculation accuracy in this work.

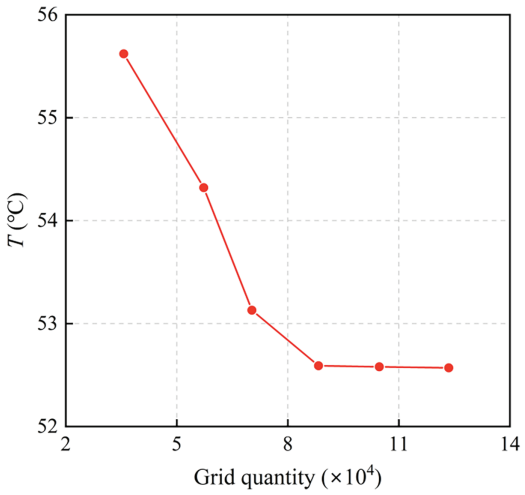

Figure 4: Grid independence test.

The model accuracy is validated using the experimental data from the previous study [30], where several temperature measurement points were set at the bottom of the TPH. The temperature variation with time was obtained in 5 s under the heating power of 360 W. The temperature data of the second measurement point (P2), as shown in Table 3, is selected as the validation data because the heat transfer process at P2, which is located in the middle of the TPH, is similar to the assumed conditions of the model. Meanwhile, the temperature variation at (15 mm, −0.31 mm) with the same room temperature and heating power is also listed in Table 3. As a result, the maximum error between the simulated and experimental values is 9.9% and the average error is 6.9%. Generally, the accuracy of the model satisfies the accuracy requirements of the subsequent study.

Table 3: Comparison of the experimental and simulated data.

Time (s)	Experimental Values (°C)	Simulated Values (°C)	Relative Error
1	25.4	23.8	6.3%
2	27.1	25.2	7%
3	28.2	26.7	5.3%
4	29.6	27.8	6.1%
5	31.3	28.2	9.9%

3 Results and Discussion

In this section, the phenomenon of internal heat transfer during pulse heating is presented in detail to provide a more in-depth understanding of the heat transfer characteristics inside a TPH. Furthermore, two critical parameters of pulse heating are analyzed: PWM and amplitude.

3.1 The Heat Transfer during Pulse Heating

The reference condition for the pulse heating process is set to a pulse frequency of 50 Hz, 50% PWM, and a heating power ($\dot{W}$) of 3.6 kW, as shown in Fig. 5. A 50% PWM indicates equal heating and non-heating durations within each pulse period. Although the TPH operates for a relatively short period with limited

time to reach the target temperature, the present work sets the heating time at 100 ms to fully observe the heat transfer process.

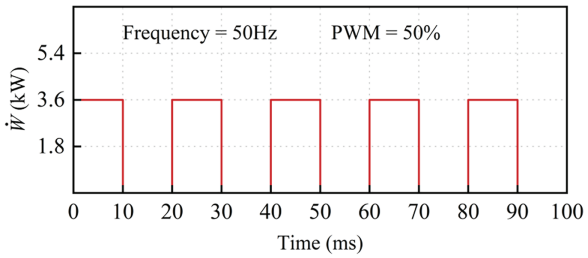

Figure 5: Pulse power waveform under the reference condition.

Temperature variation near the heat generator from 30 to100 ms is displayed in Fig. 6. In this area, the temperature tends to expand from the heat generator toward the surrounding area, resembling a glowing star pattern. This is because the thermal conductivity of the film is greater than that of glass substrate and paper, resulting in a quicker diffusion of heat and more pronounced temperature change in the film. Meanwhile, the thermal conductivity of the glass substrate is stronger than that of the paper. Thus, the temperature distribution is not symmetrical in the y-direction. When the time is 30, 50, 70, and 90 ms, the temperature of the heat generator can reach more than 330°C, while the temperature at 40, 60, 80, and 100 ms drops to about 180°C. This is because the former coincides with the heating time in one pulse period, while the latter is in the non-heating time.

Point 1 at (15 mm, 0 mm) and point 2 at (15 mm, −0.31 mm) were selected to analyze the effect of heat transfer from the heat generator to the air-paper interface during pulse heating, as shown in Fig. 7. The variation of temperature with time at these two points is demonstrated in Fig. 8. It can be seen that the two points have very different temperature variations. Since point 1 is located at the lower boundary of the heat generator, the temperature variation (T_1) is synchronized with the pulse heating period, and its maximum temperature is 355°C at 90 ms. However, the temperature of point 2 (T_2) is continuously maintaining an upward trend after 23 ms. This may be due to the paper's low thermal conductivity and high thermal inertia, which helps the paper filter out the fluctuations in heat during pulse heating and causes a delay in temperature changes at two points [23].

When the pulsed heating stops after 100 ms, T_1 cools down to 78°C after another 100 ms, however, T_2 continues to rise to 83°C as shown in Fig. 8. This is because the heat flux ($\dot{q}$) of point 2 could reach over 1.8 kW·m^{-2} after 100 ms as shown in Fig. 9. Furthermore, $\dot{q}$ of point 2 at the paper-air interface is always the maximum at different moments, because it is the closest to the heat generator. Therefore, the contact position between the paper and the TPH should be kept directly below the heat generator during printing.

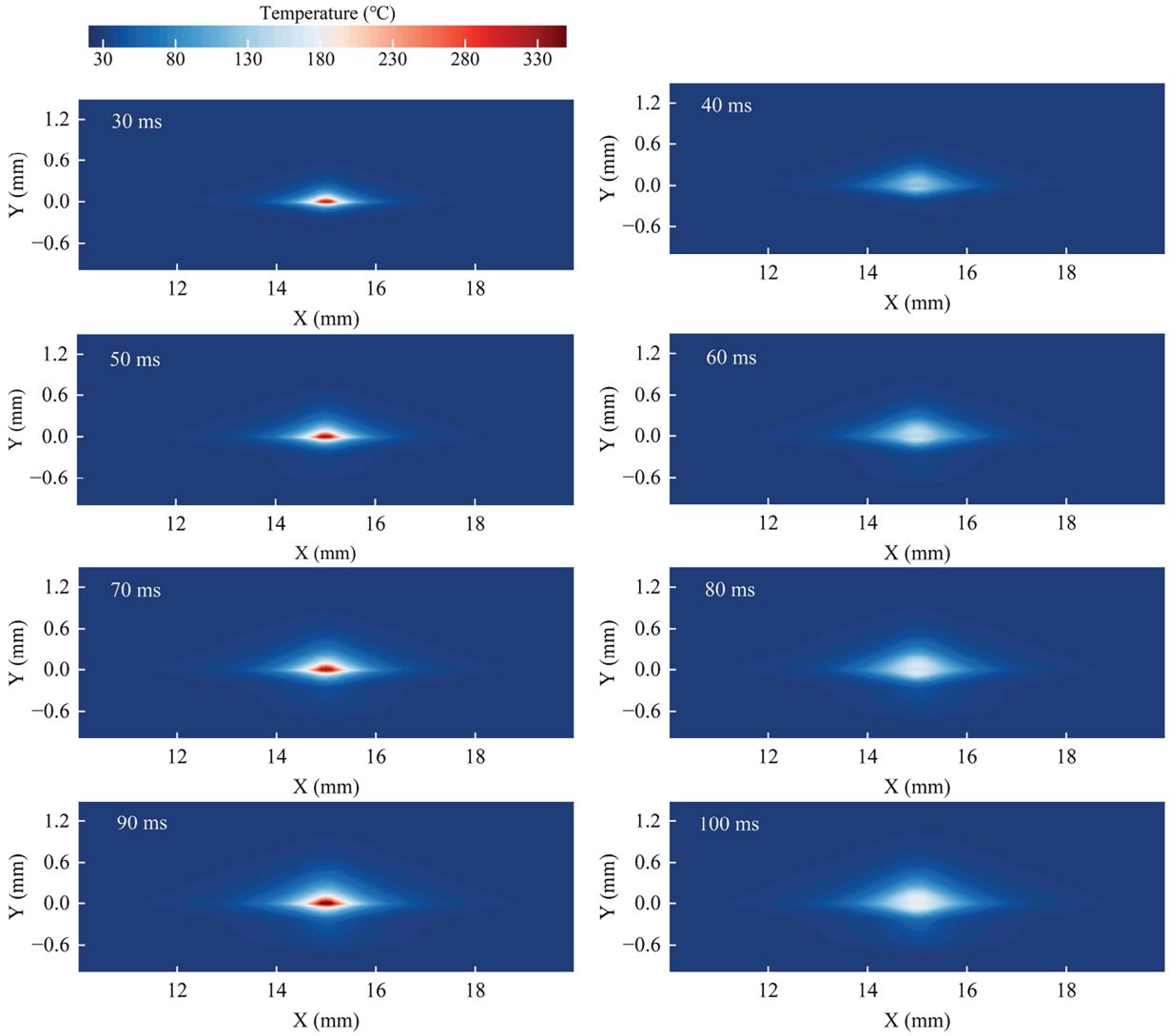

Figure 6: Temperature variation with time in the range where 10 mm ≤ x ≤ 20 mm, −1.01 mm ≤ y ≤ 1.5 mm.

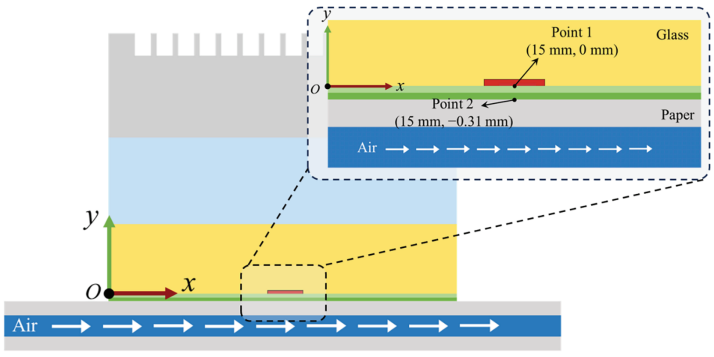

Figure 7: Position of selected points.

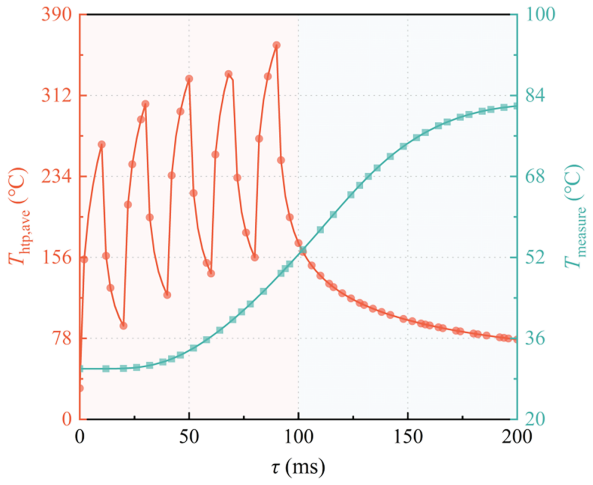

Figure 8: Variation of temperature with time at (15, 0 mm) and (15, −0.31 mm).

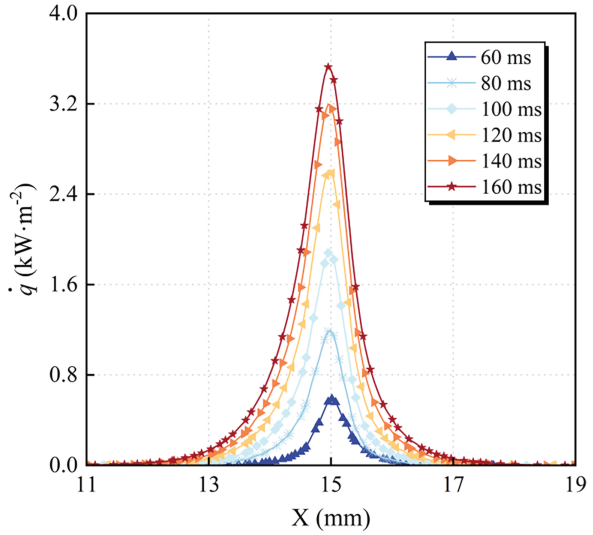

Figure 9: Heat fluxes arriving at the paper-air interface at different moments.

3.2 Effect of Various PWM

For exploring the effect of PWM variation during the pulse heating process, the temperature variation of the TPH in 100 ms is further simulated at 70%, 60%, 40%, and 30% of PWM, respectively. Fig. 10a demonstrates the heating time in each pulse period under different PWM. Essentially, the heating capacity in each period decreases as the PWM reduces. In Fig. 10b, the maximum T_1 in each pulse period also decreases with the reduction in PWM. Point 1 can reach a maximum temperature of 428°C within 100 ms at 70% of PWM, which is about 53% larger than the T_1 when the PWM is 30%.

As time is 100 ms, the temperature distribution in the y direction at x = 15 mm is shown in Fig. 11. Temperature distribution patterns remain consistent across different PWM values. Starting from point 1, the temperature increases and then decreases along the positive and negative directions of y, respectively. T_1 is lower than that in the adjacent regions because the regions around the heat generator are not heated to the same temperature during the heating process, causing that the heat generator still transfers heat to the region with lower temperature. Since the paper in the negative direction of the y-axis has a lower thermal

conductivity than the glass substrate in the positive direction of the y-axis, the temperature reduction is steeper along the negative direction of the y-axis. Meanwhile, the maximum temperature of paper is always larger than the maximum temperature of glass substrate around 4.5°C. This is because the specific heat capacity of the paper is greater than that of the glass substrate, resulting in greater thermal inertia.

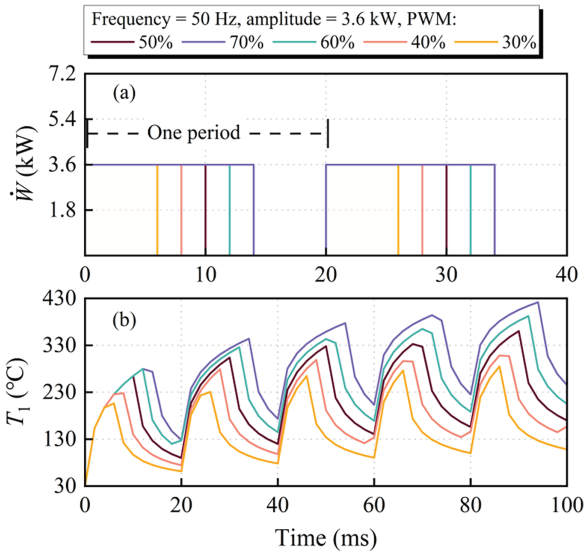

Figure 10: (**a**) Pulse heating with various PWM. (**b**) Temperature of point 1 varying over time.

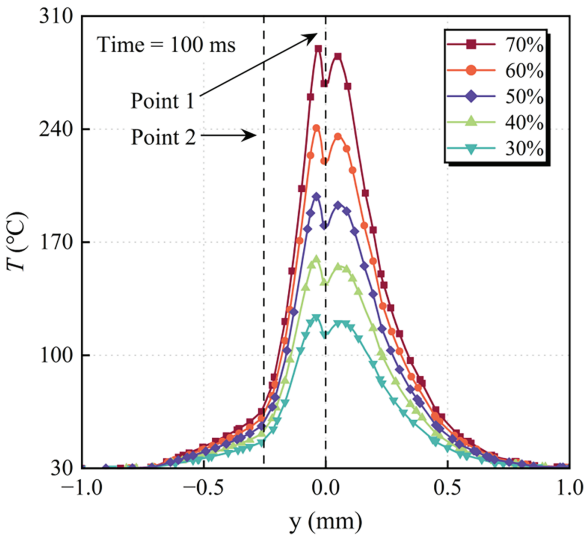

Figure 11: Temperature distribution along y direction at x = 15 mm with various PWM.

T_2 over time for different PWM is displayed in Fig. 12. The temperature remains monotonically increasing during the heating process and is not affected by the fluctuation of the pulse heating, which is consistent with the analysis in Section 3.1. Moreover, the moment when T_2 starts to change under different PWM also occurs around 23 ms. As PWM is 70%, T_2 can reach 59°C at 100 ms. When PWM is only 30%, point 2 could only be heated to 44°C.

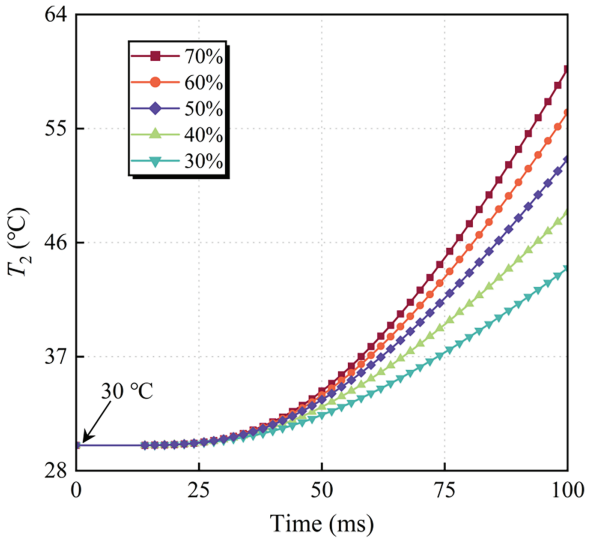

Figure 12: Temperature varying over time at point 2 under various PWM.

3.3 Effect of Various Amplitudes

The amplitude variation for each pulse heating period is shown in Fig. 13a. The maximum pulse amplitude is 5.04 kW (140% of 3.6 kW reference), while the minimum pulse amplitude is 2.16 kW (60% of reference). The variation in T_1 over a time of 100 ms is shown in Fig. 13b. Since only the amplitude is changed, T_1 has a maximum value at 90 ms for all different amplitudes. However, as the amplitude increases, the average heat capacity in each pulse period increases, thereby causing the maximum T_1 to rise. Notably, the maximum T_1 reaches 500 degrees at an amplitude of 5.04 kW, which is about 37% higher than the maximum T_1 at the reference amplitude.

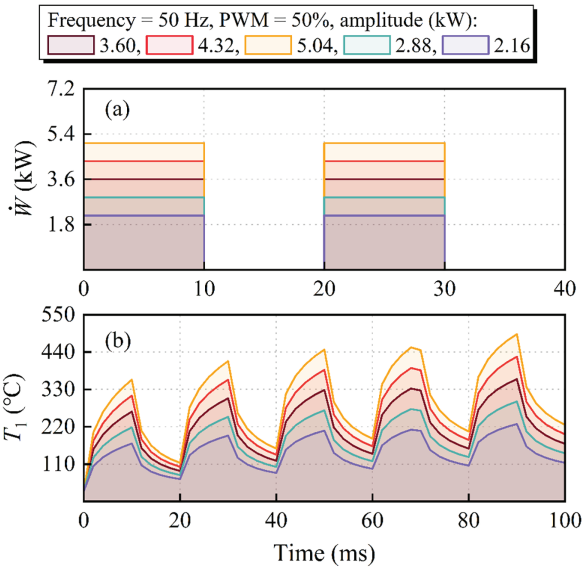

Figure 13: (**a**) Pulse heating with various amplitudes. (**b**) Temperature of point 1 varying over time.

The variation in amplitude barely changes the trend of temperature in the positive and negative directions of the *y*-axis. On the other hand, the temperature at each position increases with rising magnitude.

The highest temperature in the negative direction of the y-axis is 250°C as the amplitude is 5.04 kW, while the highest temperature in the positive direction is 242°C. In this case, the difference between the maximum temperature (ΔT) occurring in the positive and negative directions of the y-axis varies with amplitude, as demonstrated in Fig. 14. The temperature difference increases with increasing amplitude. The maximum ΔT of 7°C exceeds the minimum temperature difference of 3°C by 133%.

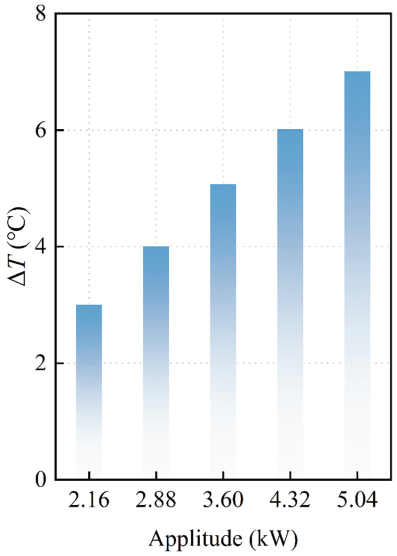

Figure 14: The difference between the maximum temperatures in both y-axis directions for different amplitudes.

4 Conclusions

In this paper, the heat transfer within the TPH is simulated and analyzed based on a reasonable heat transfer model, fully revealing the internal heat transfer characteristics of the thermal-transfer printer under pulse heating. Furthermore, parametric studies of the amplitude and PWM are carried out. The main conclusions are as follows:

(1) The temperature distribution inside the TPH during the pulse heating process resembles a glowing star pattern. One reason is that films exhibit higher thermal conductivity than other components, accelerating film temperature changes. The other reason is that the pulse heating period has heating and non-heating times.

(2) Although pulse heating causes fluctuations in the heat capacity inside the heat generator, the temperature of point 2 on the air-paper interface increases continuously. This is because the paper, with its weak thermal conductivity and large specific heat capacity, prevents fluctuations from transmitting to point 2.

(3) Increasing either the PWM or the amplitude causes the average heat capacity to rise during each pulse cycle. As a result, the internal temperature of the TPH rises at the end of any pulse heating process. Specifically, T_1 reaches a maximum of 428°C at 70% PWM, while at an amplitude of 5.04 kW, T_1 temperature reaches 500°C.

(4) Nevertheless, variations in both PWM and amplitude barely influence the shape of the temperature distribution inside the TPH. Maximum temperatures appear both directly above and below the heat generator. One is found in the paper, and the other is in the glass substrate. Meanwhile, the former's maximum temperature is higher than the latter's.

The thermal-transfer printer model has been simplified for theoretically analyzing the main heat transfer behaviors and characteristics under pulse heating conditions. Consequently, certain operational features of the thermal-transfer printer in the actual printing process might be neglected in this work. In the future research, it needs to construct a three-dimensional model of the thermal-transfer printer that conforms more to the actual printing process. On the other hand, based on the theoretical foundation of this study, the pulse heating conditions should be modified more accurately for practical printing requirements.

Acknowledgement: Not applicable.

Funding Statement: The work described in this paper is supported by Fundamental Research Funds for the National Key R&D Program of China (Grant No. 2024YFC3810000), National Natural Science Foundation of China (Grant No. 52506006).

Author Contributions: Xiufeng Fei: investigation, formal analysis, writing—original draft. Jian Liu: writing—review & editing. Dianhang Wei: methods, visualization. Xiaosong Zhang: supervision, project administration, fund acquisition, writing—review & editing. All authors reviewed and approved the final version of the manuscript.

Availability of Data and Materials: Not applicable.

Ethics Approval: Not applicable.

Conflicts of Interest: The authors declare no conflicts of interest.

Nomenclature

c	Specific heat capacity [$J \cdot kg^{-1} \cdot K^{-1}$]
P	Air pressure [Pa]
$\dot{q}$	Heat flux [$W \cdot m^{-2}$]
t	Time [ms]
T	Temperature [°C]
u	Air velocity in the x-axis direction [$m \cdot s^{-1}$]
v	Air velocity in the y-axis direction [$m \cdot s^{-1}$]
$\dot{W}$	Heating power [kW]

Greek symbols

α	Thermal diffusivity [$m^2 \cdot s^{-1}$]
ρ	Density [$kg \cdot m^{-3}$]
$\dot{\Phi}$	Heat source [W]

Acronyms

PWM	Pulse width modulation
TPH	Thermal-transfer printing head

References

1. Meng X, Tan S, Yuan Z, Zhang Y, Chen L. Experimental study on the heat transfer performance of a vapour chamber with porous wick structures printed via metallic additive manufacturing. Int Commun Heat Mass Transf. 2023;140:106496. doi:10.1016/j.icheatmasstransfer.2022.106496.
2. Cheng HP, Chiu ML. Liquid ejection characteristics of piezoelectric inkjet printhead for varied work liquids. Numer Heat Transf Part A Appl. 2007;52(9):777–93. doi:10.1080/10407780701348273.
3. Constantinescu C, Rapp L, Rotaru P, Delaporte P, Alloncle AP. Polyvinylphenol (PVP) microcapacitors printed by laser-induced forward transfer (LIFT): multilayered pixel design and thermal analysis investigations. J Phys D Appl Phys. 2016;49(15):155301. doi:10.1088/0022-3727/49/15/155301.

4. Liu Y, Liu X, Chen J, Zhang Z, Feng L. Functional toner for office laser printer and its application for printing of paper-based superwettable patterns and devices. Sci Rep. 2023;13(1):12592. doi:10.1038/s41598-023-39729-8.
5. Zhukov VI, Pavlenko AN, Shvetsov DA. The effect of pressure on heat transfer at evaporation/boiling in horizontal liquid layers of various heights on a microstructured surface produced by 3D laser printing. Int J Heat Mass Transf. 2020;163(10):120488. doi:10.1016/j.ijheatmasstransfer.2020.120488.
6. Zhou Z, Hu Z, Wang D, Wu H. Visualized-experimental investigation on the melting performance of PCM in 3D printed metal foam. Therm Sci Eng Prog. 2022;31(4):101298. doi:10.1016/j.tsep.2022.101298.
7. Zhang L, Cheng X. Heat transfer dynamics inside the Drop-on-Demand inkjet printhead with a hybrid thermal lattice Boltzmann model. Appl Therm Eng. 2019;159:113789. doi:10.1016/j.applthermaleng.2019.113789.
8. Lee HM, Lee JS. Effects of heat transfer on particle suspended Drop-on-Demand inkjet printing using lattice Boltzmann method. Appl Therm Eng. 2022;213(3):118637. doi:10.1016/j.applthermaleng.2022.118637.
9. Swain A, Chen Z, Liu Y, Wu Z, Zheng Y. Large-area ultrathin moiré chiral metamaterials by thermal-tape-transfer printing. ACS Photonics. 2023;10(5):1225–31. doi:10.1021/acsphotonics.3c00222.
10. Chae WR, Nguyen PQH, Hong JW, Lee NY. Spatially defined, high-contrast, and deformation-free dopamine subtractive thermal transfer printing using a nonelastomeric polymeric mold and its multifunctional applications. Adv Mater Technol. 2019;4(7):1800485. doi:10.1002/admt.201800485.
11. Kim HJ, Hong JP, Kwak DS, Kwon DJ. Acrylic polymer treatment on Nylon fibers improves color strength and durability in thermal transfer printing. Colloids Surf A Physicochem Eng Asp. 2021;615(1):126268. doi:10.1016/j.colsurfa.2021.126268.
12. Zhao X. Present situation and development trend of thermal transfer printer. Off Informatiz. 2017;22(8):44–5. (In Chinese).
13. Yang YJ, Choi HK, Park OO. Fabrication of silver nano-hole pattern with different hole sizes by thermal transfer printing. J Nanosci Nanotechnol. 2017;17(8):5582–6. doi:10.1166/jnn.2017.14154.
14. Duan S, Wang J, Lin Y, Hong J, Lin Y, Xia Y, et al. Highly durable machine-learned waterproof electronic glove based on low-cost thermal transfer printing for amphibious wearable applications. Nano Res. 2023;16(4):5480–9. doi:10.1007/s12274-022-5077-9.
15. Boyer A, Carter S. Laser thermal transfer printing with curable inks. NIP Digit Fabr Conf. 2000;16(1):113–7. doi:10.2352/issn.2169-4451.2000.16.1.art00030_1.
16. Kinoshita M, Hoshino K, Kitamura T. Time resolved microscopic analysis of ink layer surface in laser dye thermal transfer printing. J Imaging Sci Technol. 2000;44(6):484–90. doi:10.2352/j.imagingsci.technol.2000.44.6.art00003.
17. Kitamura T. High definition color image in dye thermal transfer printing by laser heating. In: Proceedings of the Nonlinear Image Processing 2000; 2000 Jan 22–28; San Jose, CA, USA. p. 308–16.
18. Guo R, Sun X, Yuan B, Wang H, Liu J. Magnetic liquid metal (Fe-EGaIn) based multifunctional electronics for remote self-healing materials, degradable electronics, and thermal transfer printing. Adv Sci. 2019;6(20):1901478. doi:10.1002/advs.201901478.
19. Yang Y, Chen G, Luo Z, Huang L, Zhang C, Luo X, et al. Preparation of alcohol-resistant ink using polyester resin for thermal transfer ribbon. Pigment Resin Technol. 2024;53(6):857–65. doi:10.1108/prt-12-2022-0142.
20. Luo Z, Chen G, Yang Y, Huang L, Zhang C, Luo H, et al. Preparation and properties of alcohol-resistant thermal transfer printing inks for multifunctional label printing via physical blending of resins. J Appl Polym Sci. 2024;141(6):e54930. doi:10.1002/app.54930.
21. Nitta I, Terao H, Seshita T. Analysis of contact pressure acting on a thermal print head of a thermal transfer printer. Trans Jpn Soc Mech Eng. 2004;70(693):1482–7. doi:10.1299/kikaic.70.1482.
22. Irii T, Kou M, Tsukiyama Y, Nitta I, Wauke T, Terao H. Visualization of contact patterns of thermal printhead for indirect thermal transfer printing. J Adv Mech Des Syst Manuf. 2018;12(2):JAMDSM0048. doi:10.1299/jamdsm.2018jamdsm0048.
23. Fukue T, Terao H, Hirose K, Wauke T, Hoshino H, Ito R, et al. Investigation of transient temperature response of papers in a thermal transfer printer. NIP Digit Fabr Conf. 2013;29(1):124–9. doi:10.2352/issn.2169-4451.2013.29.1.art00034_1.

24. Hirose K, Fukue T, Nakagawa F, Ito R, Wauke T, Hoshino H, et al. Basic study on transient temperature response of papers in a thermal transfer printer. In: Proceedings of the ASME, 2013 International Technical Conference and Exhibition on Packaging and Integration of Electronic and Photonic Microsystems; 2013 Jul 16–18; Burlingame, CA, USA. doi:10.1115/IPACK2013-73088.
25. Sun HM, Deng QL, Jing J. Improved design of general layout on wide format thermal transfer printing equipment. Adv Mater Res. 2013;834–836:1691–4. doi:10.4028/www.scientific.net/amr.834-836.1691.
26. Ye S, Ma J, Huang X, Wang Y, Zhang W, Tang W. Finite element simulation of thermal stress field in cutting LCD glass substrate by laser. Appl Laser. 2006;4:267–71.
27. Xu Y, Lin J, Cheng X. Quantum plasmons in single-layer boron phosphide nanostructures. J Light Scatt. 2017;29(4):325–31. (In Chinese).
28. Cui G. Numerical computation of temperature field in an LED color printer [master's thesis]. Dalian, China: Dalian University of Technology; 2010. (In Chinese).
29. Jamal B, El Moutaouakil L, Mohammed B, Abdelhalim A, Zaki Z. Numerical modeling of conjugate heat transfer through concrete hollow bricks. Heat Transf. 2023;52(5):3758–73. doi:10.1002/htj.22850.
30. Fei X, Hu H, Zhu L, Zhang X. Numerical study of the heat transfer characteristics of wide-format thermal print head. Numer Heat Transf Part A Appl. 2025;86(16):5779–94. doi:10.1080/10407782.2024.2334021.